Microstructure of compacted low-plasticity soils: the initial fabric and its evolution on stress and suction paths

Laura Gonzalez-Blanco[1,2*], *Enrique* Romero[2,1], *Núria M.* Pinyol[2] and *Eduardo E.* Alonso[2]

[1]International Centre for Numerical Methods in Engineering (CIMNE), Geomechanics Group, 08034 Barcelona, Spain
[2]Univeristat Politècnica de Catalunya (UPC), Department of Civil and Environmental Engineering, 08034 Barcelona, Spain

Abstract. Soils used in earthworks undergo different hydro-mechanical paths due to the compaction and construction process, the change in climatic conditions or the groundwater level oscillations. Their hydro-mechanical behaviour is greatly affected by their initial microstructure set on compaction that evolves differently in compliance with the stress paths. The current study investigates the differences in the initial microstructure in a low-plasticity clayey silt compacted at the dry and wet of the optimum. The microstructure was characterized by mercury intrusion porosimetry. The definition of a microstructural void ratio (e_m) inside the soil aggregates and its ratio to the total void ratio (e_m/e) allowed plotting contours of equal e_m and e_m/e in the Proctor compaction plane for the as-compacted states. Additionally, the evolution of the initial microstructure along different stress and suction paths was evaluated. The microstructural void ratio reached after the hydro-mechanical paths did not reproduce the contours of the as-compacted states in the compaction plane. In fact, the microstructural void ratio inside saturated soil aggregates follows Terzaghi's effective stress through a microstructural compressibility parameter, which provides a straightforward approach for predicting the evolution of the microstructure of compacted low-plasticity soils subjected to different stress-suction paths.

1 Introduction

It is widely recognized in the literature that microstructural features of soils set on the compaction of earthworks (road and railway constructions, dams, dykes) strongly affect their mechanical and hydraulic behaviour.

During the last decades, several advanced models incorporating microstructural information have been proposed for compacted soils [1–9] to describe the differential hydro-mechanical (HM) behaviour between soils compacted at the dry and wet sides of the optimum.

However, experimental research with microstructural characterization has mainly focused on soils of moderate to high activity [4,10–17], while the fabric evolution during different HM paths when dealing with silts and low-plasticity clays, widely found in geotechnical structures, have received less attention [8,18].

The objective of this paper is to investigate quantitatively, by using mercury intrusion porosimetry (MIP), the evolution of microstructural void ratio (e_m) along given suction-stress paths under oedometer conditions, which is very scarce for low-plasticity soils [19,20]. The suction-controlled experiments on compacted Barcelona silty clay and data from previous works [21–26] underpin a simple approach for the calculation of e_m and its evolution.

2 Experimental work

2.1 Soil tested and compaction procedure

The North Campus of UPC in Barcelona is founded on a thick Pleistocene deposit of alluvial unsaturated red silty clay with low plasticity. Over the past twenty years, several experimental programs have been carried out on this material to improve the knowledge of unsaturated soil behaviour [21–26]. The natural soil was taken from excavations located within a relatively small area (approximately 500 m by 200 m in the vicinity of the Department building). Despite the apparent homogeneity of the Pleistocene deposit, some differences in grain size distribution (sand content: 40-47%; silt content: 36-42% and clay content: 13-18%) and plasticity indexes (liquid limit: 21-32% and plastic limit: 14-20%) have been found.

Compaction curves for Standard and Modified Proctor energies are presented in Figure 1. Also indicated in the figure are the compaction conditions of the two series of samples tested at the dry (D) side of the optimum and at the wet (W) side.

The natural material was sieved (ASTM#16: 1.18 mm) and air dried under the Relative Humidity (RH) of the laboratory (RH ≅ 50%). Hygroscopic water content under such RH was 1.7%. The dry soil was mixed with distilled water to the target water content. Then it was

* Corresponding author: laura.gonzalez.blanco@upc.edu

thoroughly mixed with a spatula, adding spray water when necessary to correct evaporation losses. The mixture was left in a waterproof bag for 24 hours for homogenization.

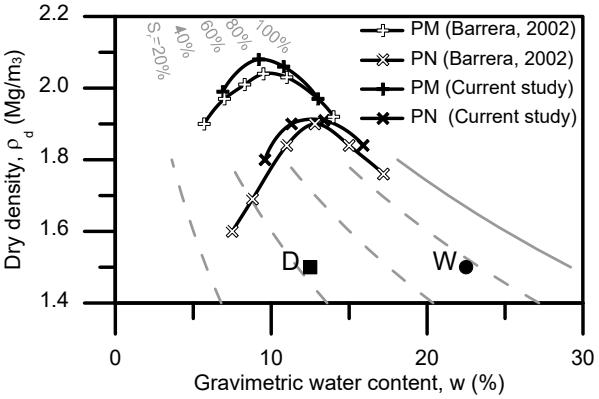

Fig. 1. Standard Proctor (SP) and Modified Proctor (MP) curves of Barcelona silty clay. Contours of equal degree of saturation (S_r) and compaction conditions of sample wet (W) and dry (D) are also indicated.

Part of the compaction load was initially applied in a greased mould using a piston travelling at a speed of 1 mm/min. Then, a more precise compaction load was applied using dead weights in an oedometer frame. The target dry density of 1.5 Mg/m^3 was achieved by a static compaction of 350 kPa for the dry samples and 30 kPa for the wet samples. Matric suction was determined after compaction with a tensiometer (T5x from UMS). A very small value (s_w = 3 kPa) was found for the wet sample. The as-compacted suction of the dry sample was s_D = 0.11 MPa. The initial stress-matric suction state is represented in Figure 2 for both samples (D and W).

2.2 Suction-controlled testing in oedometer cells

The main objective of the tests was to track the evolution of the microstructure during suction changes and loading. The applied stress-suction paths are plotted in Figure 2 for the two sets of samples. Once compacted, samples were equilibrated under the compaction stress. Then, four types of tests were performed:

- Path I: samples at the initial water content loaded to 3 MPa (DL and WL). Samples undergo matric suction reduction on loading. W sample reached saturation on loading.
- Path II: samples initially saturated and then loaded under drained conditions to 3 MPa (D_{sat} and W_{sat}).
- Path III: samples equilibrated under 0.2 MPa of matric suction and loaded at constant suction to 1.6 MPa (DDL and WDL)
- Path IV: samples equilibrated under 1 MPa of matric suction and loaded at constant suction to 1.6 MPa (DDDL and WDDL)

Finally, a water-undrained unloading path followed all tests to preserve as much as possible the microstructural network.

Loading to 3 MPa was performed in a high-stiff oedometer cell, while a suction-controlled oedometer cell was used in the rest of the tests in which the maximum load was 1.6 MPa. Matric suction was applied using the axis translation technique using a high air entry value ceramic disc of 1.5 MPa. MIP tests were performed in all the stress-suction points marked in Figure 2. Therefore, a stress path such as DDL involves an initial MIP determination in a compacted sample; another determination in a different sample equilibrated at s = 0.2 MPa; and a determination on a third sample carried at the final point of the stress path. Samples equilibrated at a given suction were removed from the oedometer and protected against drying for immediate MIP testing. MIP tests were conducted in small pieces (1 cm^3) cut from the actual oedometer specimen and then freeze-dried.

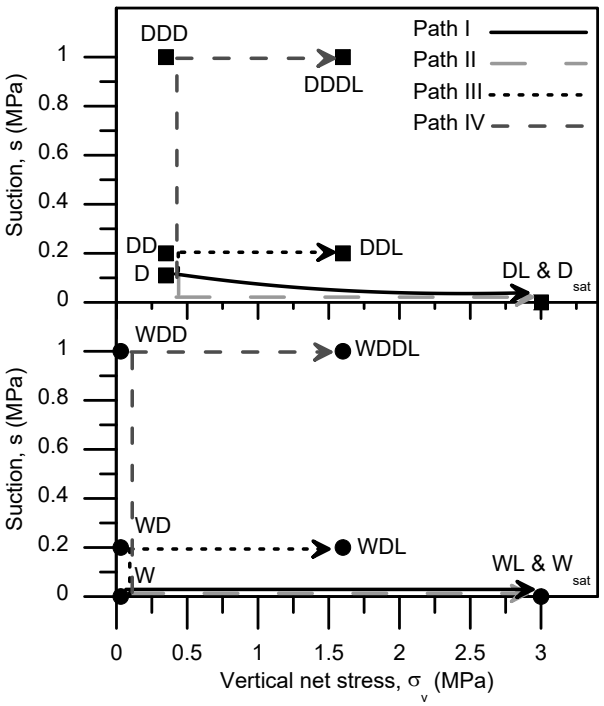

Fig. 2. Suction-stress paths in vertical net stress (σ_v)-matric suction (s) plane applied in the oedometer cell on dry compacted samples (top) and wet compacted samples (bottom).

Table 1. Water content, reference stress-suction values, void ratio, microstructural void ratio and degree of saturation at the final conditions of samples subjected to MIP tests.

State	w (%)	σ_v (MPa)	s (MPa)	e	e_m	S_r
D	12.5	0.35	0.1	0.78	0.25	0.43
W	22.5	0.03	0.003	0.78	0.30	0.77
D_{sat}	15.39	3.0	0.0	0.411	0.09	1.00
W_{sat}	15.92	3.0	0.0	0.425	0.11	1.00
DL	12.17	3.0	----	0.407	0.11	0.80
WL	15.05	3.0	----	0.408	0.15	1.00
DD	12.01	0.35	0.2	0.757	0.20	0.42
WD	15.13	0.03	0.2	0.697	0.19	0.58
DDL	11.33	1.6	0.2	0.480	0.17	0.63
WDL	11.30	1.6	0.2	0.509	0.18	0.60
DDD	9.65	0.35	1.0	0.746	0.23	0.35
WDD	10.73	0.03	1.0	0.618	0.24	0.46
DDDL	9.17	1.6	1.0	0.436	0.10	0.39
WDDL	8.70	1.6	1.0	0.536	0.185	0.43

Some changes in the pore size distribution are expected on unloading due to the unavoidable changes in stress and suction. Therefore, time intervals for MIP testing were minimized to limit these changes.

However, the best evaluation of the reliability of MIP results is to judge the consistency of results for the entire set of tests performed. This is discussed below.

2.3 Pore size distribution

MIP testing technique [27] was used by recording the intrusion-extrusion branches in all cases. Results are given for the endpoint of the paths plotted in Figure 2. Water content, void ratio, degree of saturation and stress-suction conditions at these points are given in Table 1.

MIP results are given in two related plots: accumulated volume of mercury to the total volume - non-wetting void ratio - in terms of the equivalent pore diameter (e_{nw} vs. ϕ_p) and the pore size density function (PSD) in terms of ϕ_p ($-\Delta e/\Delta\, log\ \phi_p$ vs. ϕ_p). The first plot, is useful for deriving the microstructural void ratio, e_m, and various procedures have been described [1,28,29]. In the current study, the method described in [28] based on the intrusion/extrusion curves has been selected for simplicity (e.g. Figure 3), although this criterion could underestimate the micro/macro pore size boundary [29]. Calculated values of e_m are presented in Table 1 for all the samples. The PSDs based on intrusion curves are useful to follow the evolution of pore sizes.

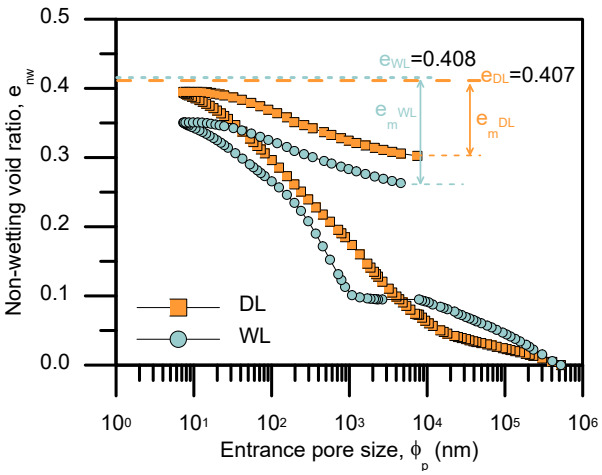

Fig. 3. Intrusion and extrusion curves used to derive the microstructural void ratio.

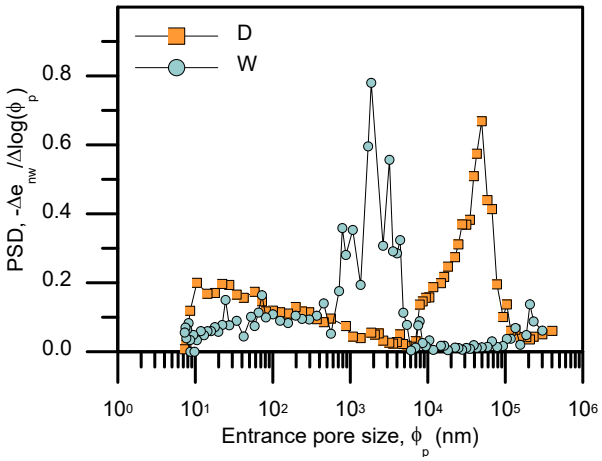

Fig. 4. PSD functions of as-compacted D and W samples.

Figure 4 shows the PSD functions of as-compacted conditions for W and D samples. The dry sample exhibits a bimodal distribution of pores. The dominant pore sizes of microvoids and macrovoids are widely different (around 50 nm vs. 60 μm). The wet sample is characterized by a unique family of pores having a dominant size around 2 μm.

The final PSD distributions of Paths I and II (referred to Fig. 2) are displayed in Figure 5 compared to the initial as-compacted state. Loading to 3 MPa (samples DL and WL) introduces significant changes in the microstructure. Large macropores of the dry sample are obliterated, and the remaining pore sizes span the range of 10 nm to 10 μm. Pores of the wet sample reduce in size and remain in an even lower range of 10 nm – 1 μm.

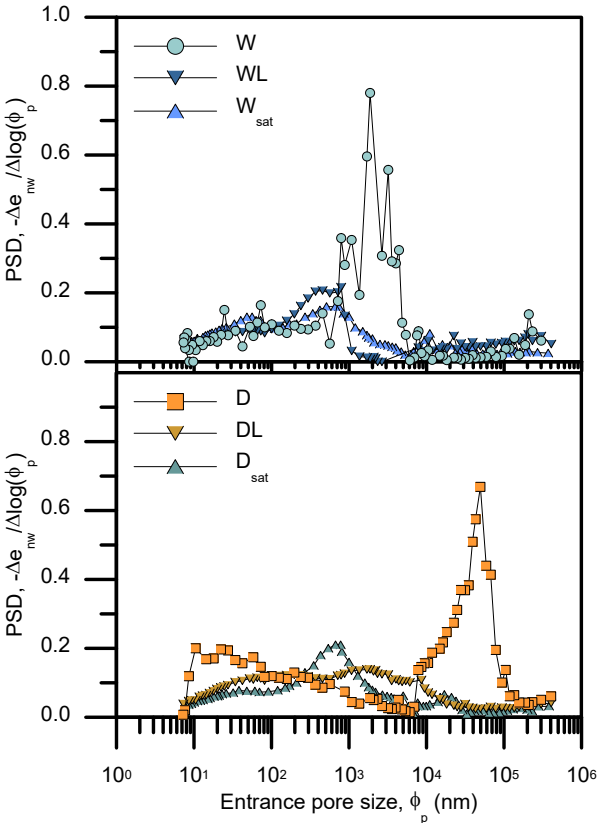

Fig. 5. PSD functions of W, WL and W_{sat} (top) and PSD function of samples D, DL and D_{sat} (bottom).

For the wet sample, the saturation and further loading to 3 MPa (W_{sat}), also reduce the pore mode of the main family of pores detected in the as-compacted conditions, reproducing a very similar shape to that after loading (WL). For the dry sample (D_{sat}), the macropores practically disappear, and the dominant pore size at the micro level increases with respect to the as-compacted conditions, being in the range of 400 nm - 1μm.

The effect of applying a moderate matric suction (200 kPa) is shown in Figure 6. The pore size distribution of the dry sample remains essentially unchanged. However, the wet sample experiences a more significant change in suction, from an initial value of 3 kPa to a final value of 200 kPa. Two effects are observed: (a) a family of inter-aggregate large pores has developed in the range 50–300 μm, and (b) the dominant family of pores has reduced from an original mean size of 2 μm to a smaller size of 1 μm.

Loading the previously dried samples to s = 200 kPa to a vertical total stress of 1.6 MPa reduces the size of

all pores in both dry (DDL) and wet (WDL) samples (Fig. 6). Interestingly, both samples retain a bimodal distribution of pore sizes.

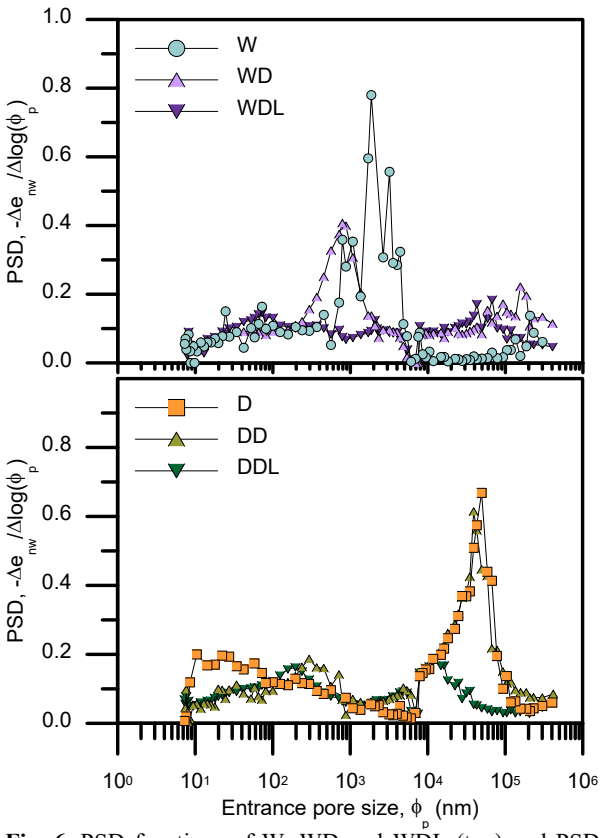

Fig. 6. PSD functions of W, WD and WDL (top) and PSD function of samples D, DD and DDL (bottom).

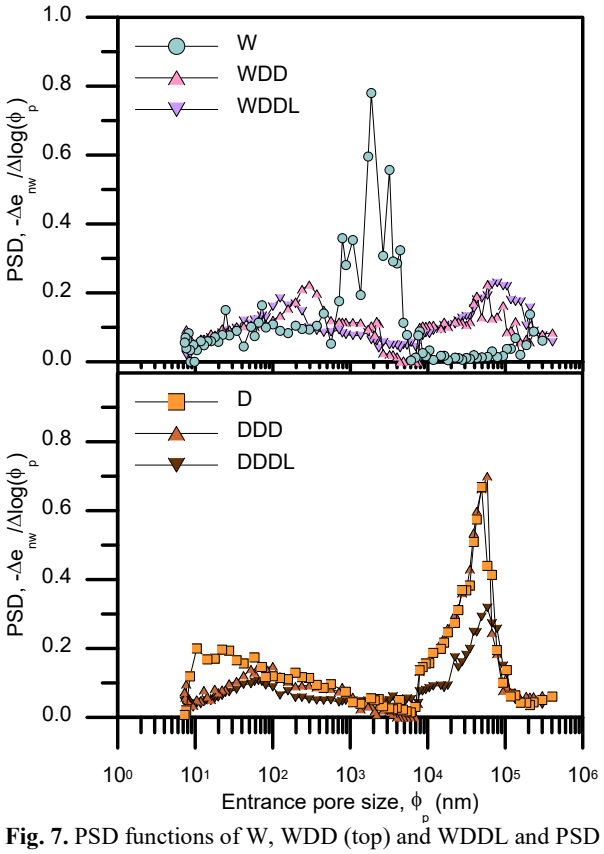

Fig. 7. PSD functions of W, WDD (top) and WDDL and PSD function of samples D, DDD and DDDL (bottom).

Samples dried to a high suction (1 MPa) (samples DDD and WDD in Fig. 7) exhibited trends similar to the effects observed in drying to 200 kPa. The dry sample did not experience significant changes in pore size distribution. In contrast, the wet sample experienced a more intense reduction in the size of small pores, and a family of large pores developed.

The application of a vertical stress (1.6 MPa) to the previously dried samples to 1 MPa of matric suction maintained the bimodal distribution of pore sizes in both cases (Fig. 7). Sample DDDL experienced a reduction of the size of larger and smaller pores. This was also the case with the WDDL sample but to a lesser extent.

A general trend can be drawn by observing the PSDs. Samples compacted at dry conditions maintain a significant macroporosity provided some non-negligible suction is present in the soil. Macropores collapse only under saturated conditions and at high confining stress (3 MPa). The microstructure of the samples compacted at dry conditions do not experience significant changes within the range of suctions (0–1 MPa) and stresses (0–3 MPa) applied.

In the case of samples compacted on the wet side, the drying process results in the development of macroporosity, even to moderate suctions (200 kPa). Microvoid size reduces in all the stress paths implying a suction increase. The relevant result is that suction creates a bimodal pore structure in samples initially characterized by a monomodal fabric.

3 Microstructural state variables and their evolution

3.1 Microstructure set on compaction

The microstructural void ratio, calculated as proposed in Figure 3, was determined for the compaction conditions of Barcelona silty clay together with data reported by several authors [21–26]. The results are summarized in Figure 8. Contours of constant e_m are also given in the plot. e_m is shown to increase with compaction water content and to decrease with attained dry density. Despite the actual heterogeneity in grain size distribution and plasticity in the original references, a reasonably consistent distribution of e_m in the compaction plane is obtained for the different results.

Figure 8 also provides information on the contours of the microstructural state variable $\xi_m = e_m/e$ [5], which approximately follow contours of equal S_r. . ξ_m increases with compaction water content and dry density. Contours of ξ_m in Figure 8 are qualitatively similar to equivalent contours presented by [5] based on e_m data reported by [30] for compacted high-plasticity Boom Clay. In the case of Boom Clay, e_m was essentially controlled by compaction water content and the effect of achieved density was minor. The results indicate that compaction conditions lead, for a given soil, to a microstructural state, smoothly varying in an ordered manner in the compaction plane.

3.2 Microstructure evolution against suction and stress paths

An obvious step now is to investigate if dry density and water content states reached by stress and suction paths, but not by the compaction process, would reproduce the contours given in Figure 8. The experiments performed provided data in this regard. Figure 9 shows the measured e_m associated with the void ratio and water content reached after the application of a particular suction-stress path starting at the initial compaction conditions. A rapid evaluation of the figure indicates that the state variable contours in Figure 8 are far from explaining the results in Figure 9. The wetting of samples and the subsequent static compaction is a fundamentally different process if compared with the application of suction and stress changes to a previously compacted sample. In fact, the initial compaction state tends to be preserved to a certain degree if stress and suction changes are applied.

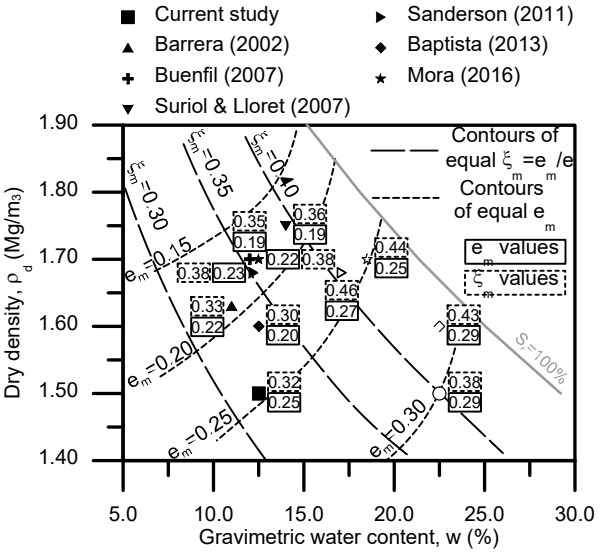

Fig. 8. Values of micro void ratio (e_m) and microstructural state variable ($\xi_m = e_m/e$) of different compacted samples of Barcelona silty clay and contours of equal e_m and ξ. Filled symbols: samples compacted dry; empty symbols: samples compacted wet.

Therefore, the approach to predict the fabric of a given soil state requires a different methodology, which may be divided into two steps: first, the initial as-compacted state should be determined. This information is given in Figure 8. In the second step, a procedure has to be devised to estimate the evolution of e_m and e during stress and suction changes.

The evolution of e_m and e is naturally linked to constitutive soil modelling. This is the case of changes in the void ratio, which are explained by total volumetric deformations. But changes in e_m based on constitutive approaches to predict microstructural deformations have seldom been reported. A notable exception is the work of [2] where e_m was linearly related to the water ratio.

A different approach is presented here in line with the recent publication of [9]. It is inspired by the assumed behaviour of clay aggregates described in [31] in connection with the behaviour of expansive clays. It was expected that clay aggregates should obey the Terzaghi effective stress because they would be most likely saturated. For an average pore diameter of 0.1 μm, which characterizes the micro void size, an air entry value close to 3 MPa is calculated. This is a high value uncommon in engineering applications.

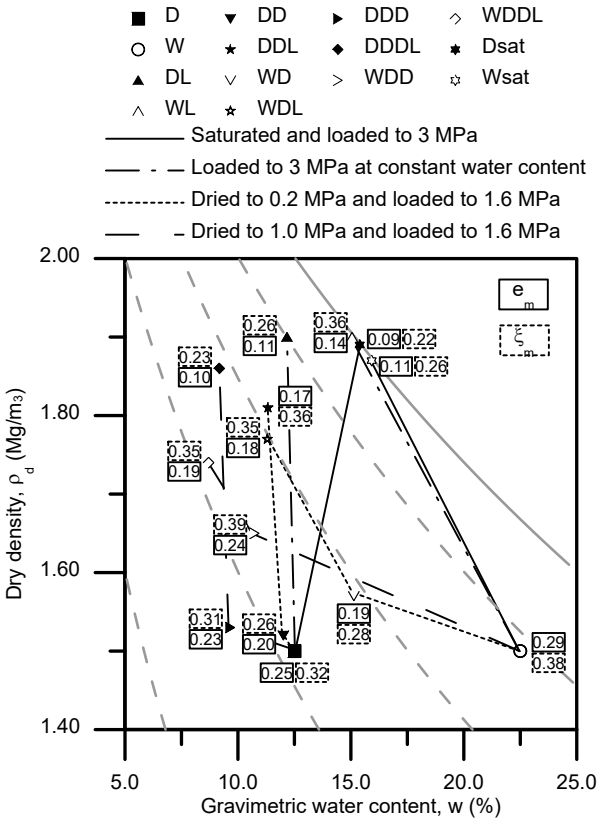

Fig. 9. Values of micro void ratio (e_m) and microstructural variable (ξ_m) of samples after different stress/suction paths in the compaction plane.

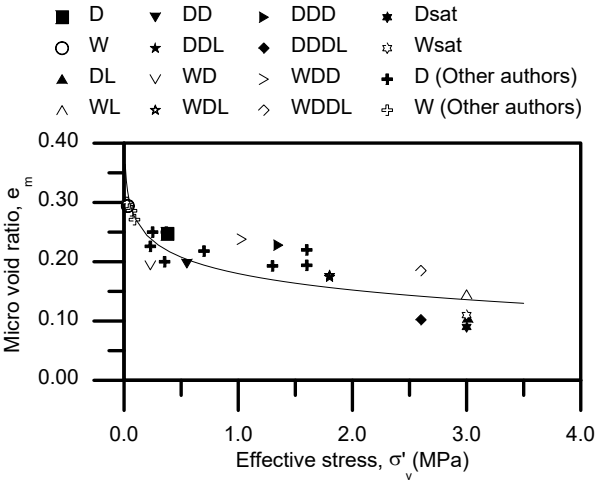

Fig. 10. Relationship between Terzaghi's effective stress and micro void ratio (e_m) measured in different samples.

Measured e_m values at the positions shown in Figure 2 are plotted in terms of the effective stress ($\sigma'_v = \sigma_v + s$) in Figure 10. In addition, data interpreted from test results published by [21–26] are included in the plots. The figure also shows a logarithmic expression fitting the data, providing a reasonably good fit for the range of effective stresses plotted (0.05-3 MPa). The compressibility equation for the microstructure of the compacted Barcelona silty clay is:

$$e_m = e_{mo} - \kappa_m \, ln \, \frac{\sigma'_v}{\sigma'_{vo}} \quad (1)$$

where e_{mo} = 0.18, σ'_{vo} = 1 MPa and κ_m = 0.04 are fitting parameters.

4 Summary and concluding remarks

The microstructure of compacted soils and its evolution along hydro-mechanical paths have been studied for active clays in the last decades; however, its relevance in silts and low-activity clays has been less explored. The current study investigates the microstructure changes in a low-plasticity clayey silt due to the application of different stress and suction paths typically affecting earthworks.

Samples were statically compacted at the dry and wet sides of the optimum at the same dry density. The vertical stress-matric suction paths were performed in a controlled-suction oedometer using the axis translation technique. The microstructure at the different states (as-compacted and after HM paths) was determined using MIP. The definition of a microstructural void ratio (e_m) inside the soil aggregates and its ratio to the total void ratio (e_m/e) allowed plotting contours of equal e_m and e_m/e in the Proctor compaction plane for the as-compacted states. Samples compacted at the wet side of optimum exhibit a higher microstructural void ratio. Drier conditions of compaction and higher compaction energy lead to a reduction of this microstructural void ratio. These results are equivalent to the ones reported in high-plasticity clays. However, the microstructural void ratio reached by stress and suction paths did not reproduce the contours in the compaction plane. The preparation of samples by adding water and the subsequent static compaction is a different process if compared with applying suction and stress paths on a previously compacted sample.

In fact, the initial compaction state tends to be preserved to a certain degree when stress and suction changes are applied. For these paths, it was expected that clay aggregates should obey the Terzaghi's effective stress because they would be most likely saturated. Therefore, the microstructural void ratio would change with changes in suction and/or stress, as has been observed. Experimental data was used to determine a microstructural compressibility coefficient. This effective stress-based methodology provides a straightforward and reliable approach for predicting the evolution of the microstructural void ratio of compacted low-plasticity soils subjected to different stress-suction paths.

References

1. E. Romero, G. Della Vecchia, C. Jommi, Géotechnique **61** (4), 313–328 (2011)
2. E. Romero, Eng. Geol. **165**, 3–19 (2013)
3. R. Hu, Y. F. Chen, H. H. Liu, C. B. Zhou, Geotechnique **63** (16), 1389–1405 (2013)
4. Q. Wang, Y. J. Cui, A. M. Tang, J. D. Barnichon, S. Saba, W. M. Ye, Eng. Geol. **164**, 67–76 (2013)
5. E. E. Alonso, N. M. Pinyol, A. Gens, Géotechnique **63** (6), 463–478 (2013)
6. G. Della Vecchia, A. C. Dieudonné, C. Jommi, R. Charlier, Int. J. Numer. Anal. Methods Geomech. **39**, 702–723 (2015)
7. Y. Qiao, Y. Xiao, L. Laloui, W. Ding, M. He, Comput. Geotech. **115**, 103173 (2019)
8. A. Azizi, G. Musso, C. Jommi, Can. Geotech. J. **57** (1), 100–114 (2020)
9. P. Yin, S. K. Vanapalli, Can. Geotech. J. **59** (9), 1602–1621 (2022)
10. A. Lloret, M. V. Villar, M. Sànchez, A. Gens, X. Pintado, E. E. Alonso, Geotechnique, **53** (1), 27–40 (2003)
11. E. E. Alonso, E. Romero, C. Hoffmann, E. García-Escudero, Eng. Geol. **81** (3), 213–226 (2005)
12. H. Nowamooz, F. Masrouri, Eng. Geol. **106** (3–4), 105–115 (2009)
13. C. A. Farulla, A. Ferrari, E. Romero, Can. Geotech. J. **47** (6), 688–703 (2010)
14. R. Monroy, L. Zdravkovic, A. Ridley, Geotechnique **60** (2), 105–119 (2010)
15. E. Romero, G. Della Vecchia, C. Jommi, Geotechnique **61** (4), 313–328 (2011)
16. G. J. Burton, J. A. Pineda, D. Sheng, D. Airey, Eng. Geol. **193**, 363–373 (2015)
17. H. Trabelsi, E. Romero, M. Jamei, Appl. Clay Sci. **162**, 57–68 (2018)
18. F. Casini, J. Vaunat, E. Romero, A. Desideri, Acta Geotech. **7** (2), 139–150 (2012)
19. O. Cuisinier, L. Laloui, Int. J. Numer. Anal. Methods Geomech. **28** (6), 483–499 (2004)
20. A. Koliji, L. Vulliet, L. Laloui, Can. Geotech. J. **47** (3), 297–311 (2010)
21. M. Barrera, PhD Thesis, Universitat Politècnica De Catalunya (2002)
22. C. M. Buenfil, PhD Thesis, Universitat Politècnica De Catalunya (2007)
23. J. Suriol, A. Lloret, Ing. Civil **147**, 1–10 (2007)
24. V. Sanderson, Ms Thesis, Universitat Politècnica De Catalunya (2011)
25. E. A. Baptista, Ms. Thesis, Universitat Politècnica De Catalunya (2013)
26. R. S. Mora, PhD Thesis, Universitat Politècnica De Catalunya (2016).
27. E. Romero, P. H. Simms, Geotech. Geol. Eng. **26**, 705–727 (2008)
28. P. Delage, G. Lefebvre, Can. Geotech. J. **21**, 21–23 (1984)
29. S. Yuan, X. Liu, E. Romero, P. Delage, O. Buzzi, Geotech. Lett. **10**, 1-7 (2020)
30. V. Merchán, PhD Thesis, Universitat Politècnica de Catalunya (2011).
31. E. E. Alonso, J. Vaunat, A. Gens, Eng. Geol. **54**, 173–183 (1999)